Spectral and structural signatures of phase transformation in the charge density wave material $1T$-TaS_2 intercalated with triethylenediamine

M. K. Kinyanjui,[1] J. Holzbock,[2] J. Köster,[1] C. Singer,[3] M. Krottenmüller,[3] M. Linden,[2] C. A. Kuntscher,[3] and U. Kaiser[1]
[1]*Central Facility of Electron Microscopy, Ulm University, Albert-Einstein Allee 11, 89081 Ulm, Germany*
[2]*Institut für Anorganische Chemie II, Ulm University, Albert-Einstein-Allee 11, 89081 Ulm, Germany*
[3]*Experimental Physics II, Institute of Physics, University of Augsburg, Universitätsstr. 1, 86159 Augsburg, Germany*

(Received 10 October 2019; revised 10 December 2020; accepted 19 January 2021; published 9 February 2021)

Many transition-metal dichalcogenides show competing metallic, superconducting, charge density waves (CDWs), or Mott-insulating phases. Understanding the interplay between these phases is of fundamental interest. One approach to understand this relationship is to suppress one or more of the competing phases through systematic introduction of disorder. Intercalation is one of several approaches used to introduce this disorder. However, the intercalation process itself and the resulting changes in the atomic and electronic structure of the host-intercalant systems are not completely understood. Here, we characterize the structural and spectral signatures accompanying the intercalation of triethylenediamine [TED, $(C_6H_{12}N_2)$] into the CDW material $1T$-TaS_2. Electron diffraction and electron microscopy imaging reveal that the intercalation of TED into $1T$-TaS_2 leads to a change of the layer stacking in the intercalated TaS_2-TED structure. Increased peak intensity is also observed between 3–5 eV in the valence electron-energy-loss spectra of the intercalated sample. Using electronic structure and theoretical spectra calculations we argue that these spectral features are a result of the band-structure changes due to structural phase transformation accompanying intercalation.

DOI: 10.1103/PhysRevB.103.064101

I. INTRODUCTION

$1T$-TaS_2 is a quasi-two dimensional (2D) layered material characterized by charge density waves (CDWs) which are a periodic modulation of the valence charge density [1–5]. The CDW modulation is also accompanied by a periodic lattice distortion (PLD) which is a periodic modulation of atomic positions. A CDW can be described as [6]

$$\rho(\boldsymbol{r}) = \rho_0 + \rho_l \cos(\boldsymbol{q}.\boldsymbol{r} + \varphi(\boldsymbol{r})), \tag{1}$$

where $\rho(\boldsymbol{r})$ is the modulated charge density, ρ_0 is the background charge density, ρ_l is the CDW amplitude, $\boldsymbol{q}$ is the wave vector of the CDW, and $\varphi(\boldsymbol{r})$ is the CDW phase. The modulation wave vector can be given by $\boldsymbol{q} = 2\boldsymbol{k}_F$ where $\boldsymbol{k}_F$ is the Fermi wave vector. The CDW can be probed directly using scanning tunneling microscopy methods [7]. Diffraction and imaging techniques such as high-resolution and scanning transmission electron microscopy [HR(S) TEM] [8–10], electron [1,5], neutron, and x-ray diffraction [11–13], are on the other hand sensitive to the structural modulation arising from the PLD. Strong CDW/PLD modulations are observed in some metallic 1D conductors and 2D transition-metal dichalcogenides (TMDCs) [1,14] In most cases, the structure and commensuration of the CDW varies with temperature, structural polytype, doping, intercalation, strain, pressure, and dimensionality [1]. Structural polytypes, mainly a characteristic of the 2D TMDCs, are classified into two groups depending on the coordination of the central transition-metal ion and layer stacking. These include the trigonal-prismatic cocoordinated polytypes such as the $3R$, $2H$, the mixed polytypes $4Hb$, $6R$ consisting of both octahedral and trigonal-prismatic layers, as well as the octahedral coordinated $1T$ polytypes [1,15,16].

The $1T$-TaS_2 polytype, which is the focus of this paper, undergoes three CDW transitions as a function of temperature. This includes an incommensurate phase below 550 K, the nearly commensurate (NC-CDW) phase below 350 K, and commensurate (C-CDW) phase below 180 K [1]. There have been considerable efforts directed towards understanding the properties of $1T$-TaS_2 and other related CDW materials [1,4,6,14]. It has been shown that CDW competes with superconductivity in many strongly correlated materials [17–20]. Understanding the intricate interplay between different ordered electronic states has therefore become a key goal in solid-state research [19–22]. In particular, it has been shown that the use of controlled disorder introduced through intercalation, doping, or irradiation can change the intricate balance between these competing orders [1,21,23,24]. However, this also leads to the necessity to understand how this controlled disorder affects the nature and the structure of the ordered states under study.

The layered nature of $1T$-TaS_2 allows for the intercalation of metal ions and organic molecules within the van-der Waals gap and is associated with charge transfer from the intercalate to the host structure [1,24–35]. This intercalation process can lead to large changes in the nature of the CDW state, the CDW transition temperature, superconductivity, metal-insulator transitions, and magnetic properties of CDW materials [1,24,27,35–37]. The nature of the intercalation process in these structures therefore remains an active

topic of interest due to large number of changes observed both in the host structure and in the intercalate. In this regard, intercalated $1T$-TaS_2 structures have revealed changes in the spectral properties below 1 eV associated with intercalation [25,27,29]. These were associated with changes in the free-carrier excitations due to charge transfer during the intercalation process [25]. The influence of intercalation on spectra has been variously interpreted as arising from the charge-transfer process as well as a superposition of the optical properties of the intercalant and the host [25,36,37]. It is now known that intercalation can lead to structural phase transformation due to changes in the stacking arising from the intercalant [1,24,28,32]. The influence of such phase transformations on the high-energy spectra are less well known. In this paper, we have investigated atomic and electronic structural changes of $1T$-TaS_2 accompanying the intercalation with triethylenediamine (TED) molecules as well as the subsequent modifications of the CDW structure. In particular, we show and interpret how the valence electron-energy-loss spectrum (VEELS) is modified by the intercalation process. VEELS refers to the spectral region of an EELS spectrum ($\Delta E < 50$ eV) dominated by interband transitions, excitons, and collective plasmon excitations.

II. EXPERIMENTAL METHODS

Intercalation was performed using TED samples purchased from Sigma-Aldrich and a $1T$-TaS_2 single crystal purchased from Graphene HQ. These were then sealed in a glass ampoule and heated at 300 °C for 8 h. After the intercalation, the intercalated sample was removed from the glass ampoule and prepared for TEM investigations. In order to confirm the success of the intercalation process, room-temperature infrared reflectivity measurements and EELS were used to detect the TED molecules within bulk TaS_2 flakes and thin TaS_2 layers, respectively. Room-temperature infrared reflectivity measurements were carried out in the frequency range $\approx$ 100–24000 cm^{-1} with an infrared microscope (Bruker Hyperion), equipped with a 15× Cassegrain objective, coupled to a Bruker Vertex v80 Fourier-transform infrared spectrometer. The intensity reflected from an Al mirror served as reference. Very thin layers from pristine and intercalated TaS_2 were prepared using mechanical exfoliation for TEM experiments. These layers were then transferred onto perforated carbon sample grids for TEM investigations. TEM investigations were done on freestanding layers lying on top of a hole in the supporting TEM sample grids. EELS spectra were acquired using a Gatan-Tridiem spectrometer attached to a Titan 80–300-kV TEM and operating at 80 kV. Short exposure times on the order of 0.05–0.1 s were used during the acquisition of the VEELS spectrum. Electronic structures and spectra calculations were obtained within the full potential linearized augmented plane-wave approximation implemented in WIEN2K code. No geometrical optimization was done during the calculation. Muffin tin radii of 2.5 and 2.08 were used for Ta and S, respectively. The number of K points and the value of $R - K_{max}$ were varied in order to achieve total convergence. The convergence criteria charge convergence ($e-$) and energy convergences (Ry) were both set to 0.0001. The converged parameter $R_{mt}K_{max}$ was set to 7, where R_{mt} is the smallest atomic sphere radius in the unit cell and K_{max} is the magnitude of the largest K vector. 130 k points in the irreducible Brillouin zone (IBZ) were used. To calculate the optical properties and simulate EELS spectra, the dielectric tensor was calculated using the OPTIC package which is included in the WIEN2K code. A denser mesh of 300 k points in the IBZ were used during the calculation of the optical properties. A single scattering EELS spectrum is proportional to the energy loss function, $\mathrm{Im}\{\frac{-1}{\varepsilon(q,\omega)}\}$ as given by

$$\mathrm{Im}\left\{\frac{-1}{\varepsilon(q,\omega)}\right\} = \frac{\varepsilon_2(q,\omega)}{\left[\varepsilon_1^2(q,\omega)+\varepsilon_2^2(q,\omega)\right]}, \tag{2}$$

where $\varepsilon(q,\omega) = \varepsilon_1 + i\varepsilon_2$ is the dielectric function with ε_1 and ε_2 being the real and imaginary parts of the dielectric function, respectively [38–40]. In the density-functional approach, the imaginary part of the dielectric tensor, ε_2 is obtained as

$$\varepsilon_2^{ij}(\omega) = \frac{4\pi^2 e^2}{m^2\left(\omega - \frac{\Delta C}{\hbar}\right)^2}\sum_{i,f}\int_{BZ}\frac{2dk}{(2\pi)^3}|\langle v_k|p_j|c_k\rangle||\langle c_k|p_i|v_k\rangle| \times \delta(E_{ck}(k) + \Delta C - E_{vk}(k) - \hbar\omega), \tag{3}$$

where $|v_k\rangle$ and $|c_k\rangle$ are states in the valence and conduction bands, respectively [41]. The corresponding band energies are E_{vk} and E_{ck}, respectively. Real part of the dielectric function ε_1 and energy loss function, ELF, are then obtained using the Kramers-Kronig transformation. Interband transitions between $|c_k\rangle$ and $|v_k\rangle$ states arising from different bands contribute to the peaks observed in ε_2. In addition, partial ε_2 functions can be calculated as implemented in WIEN2K by taking contributions from a pair or a group of valence and conduction bands contributing to peaks in the ε_2 function.

III. RESULTS AND DISCUSSION

A. Core-loss EELS and infrared reflectivity

The first step was to confirm the presence of intercalated TED molecules. Therefore, we performed infrared-spectroscopy investigations on bulk intercalated flakes which was then complemented by local core-loss EELS investigations on free-standing, intercalated thin layers. Core-loss EELS was conducted at C-K and N-K edges of the $C_6H_{12}N_2$ molecule in the intercalated TaS_2 layer (TaS_2-TED). In Fig. 1(a) we display the core-loss spectra obtained at the C-K edge of a thin TaS_2-TED layer (solid curve). Similarly, the core-loss peak obtained at the N-K edge is displayed in Fig. 1(b). The presence of these C- and N-K edge EELS signals arising from the C and N atoms in the $C_6H_{12}N_2$ molecule demonstrate the success of the intercalation into $1T$-TaS_2. This was confirmed using infrared spectroscopy, as shown in Fig. 2 where infrared reflectivity results from TED intercalated (solid line) and pristine $1T$-TaS_2 flakes (dashed-dotted line) are compared.

In Fig. 2 the infrared reflectivity spectra are shown for ranges (a) 100–20 000 cm^{-1}, (b) 100–600 cm^{-1}, (c) 600–1800 cm^{-1}, (d) 2600–3400 cm^{-1}, respectively. The frequency range 2600–3400 cm^{-1} is dominated by frequencies arising from C-H stretching modes [see Fig. 2(d)]. The frequencies observed in the range 800–1300 cm^{-1} on the other hand have their origin in C-N, C-N-C modes of the $C_6H_{12}N_2$

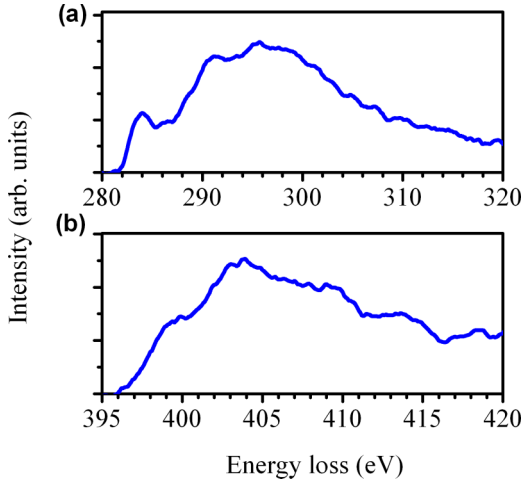

FIG. 1. Core-loss electron-energy-loss spectra obtained at (a) C-*K* edge (b) N-*K* edge of the TED molecule ($C_6H_{12}N_2$) intercalated in TaS_2.

molecule [42–44]. Since the reflectivity measurements were carried out on an as-grown TED intercalated crystal, we refrain from a quantitative analysis of the overall reflectivity spectrum. However, we note that both infrared and EELS spectroscopic results confirm the presence of intercalated TED molecules between TaS_2 layers.

B. Structural results of the intercalation process

To shed light on the structural effects of the intercalation process, electron diffraction and HRTEM measurements were then carried out on intercalated thin layers. Figure 3(a) displays an electron diffraction pattern of $1T$-TaS_2 obtained at 300 K. The diffraction pattern shows the main reflections originating from $1T$-TaS_2 main structure (marked with open circles) and the superlattice reflections (marked with solid triangles). The superlattice spots are due to the CDW/PLD modulation accompanying the NC-CDW characteristic of the $1T$-TaS_2 at 300 K. The NC-CDW pattern in $1T$-TaS_2 arises from three CDW/PLDs with a wave vector $\mathbf{q_{nc}} \sim 0.245\,\boldsymbol{a}_0^* + 0.068\,\boldsymbol{b}_0^* + \frac{1}{3}\,\boldsymbol{c}_0^*$ and rotated 12° from the $\langle 10\bar{1}0\rangle$ direction [1,4].

In Fig. 3(b) we display the electron diffraction pattern for TaS_2-TED obtained at 300 K. For comparison the electron diffraction patterns for $1T$-TaS_2 obtained at 90 K and $2H$-TaS_2 are also shown in Figs. 3(c) and 3(d), respectively. In contrast to $1T$-TaS_2, $2H$-TaS_2 does not show CDW/PLD modulation at 300 K. Therefore its diffraction pattern is only characterized by main structure spots without the superlattice spots. When $1T$-TaS_2 is cooled down to 90 K it locks into the C-CDW state characterized by a $\sqrt{13}\,a_0^* \times \sqrt{13}\,a_0^*$ superlattice. The zoomed electron diffraction patterns for $2H$-TaS_2, NC-CDW $1T$-TaS_2, and TaS_2-TED are displayed in Figs. 3(d)–3(f), respectively. In Fig. 3(g) we also show the zoomed diffraction characterized by superlattice spots $\boldsymbol{q}_c$ due to the C-CDW obtained when the pristine NC-CDW

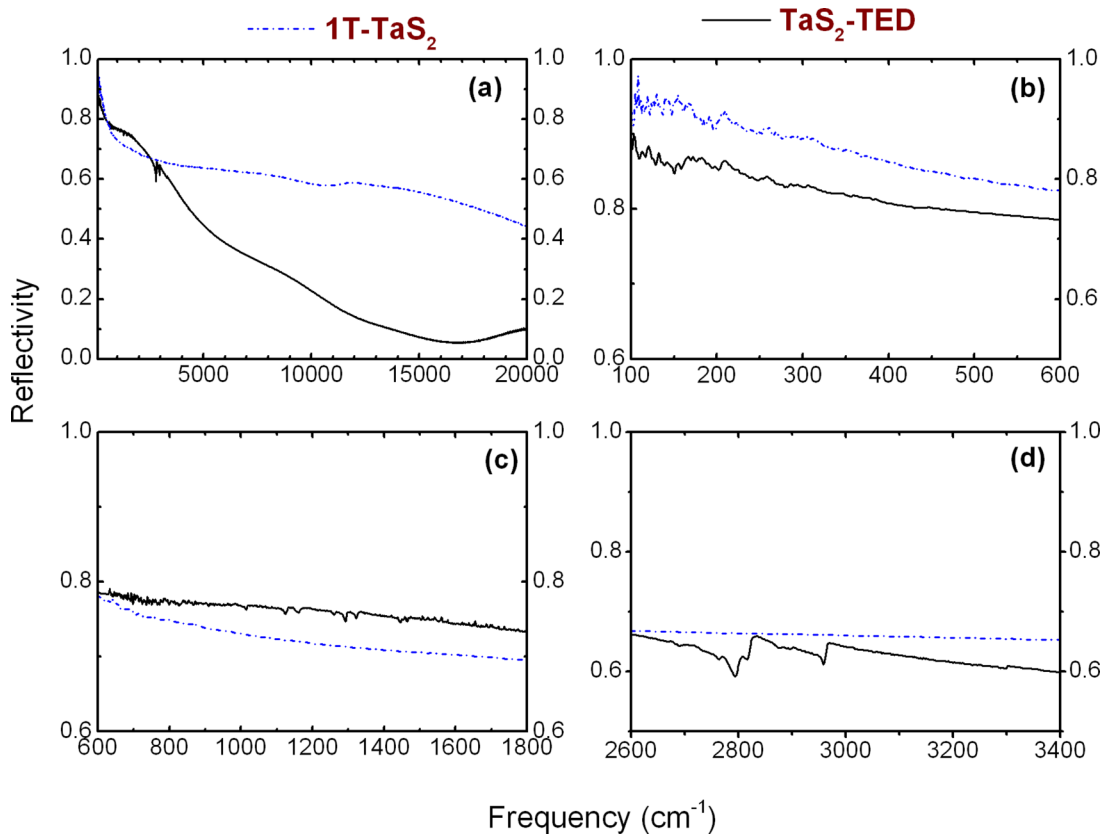

FIG. 2. Infrared reflectivity for pristine $1T$-TaS_2 (dashed-dotted) and TaS_2-TED (solid line) for ranges (a) 100–20 000 cm^{-1}, (b) 100–600 cm^{-1}, (c) 600–1800 cm^{-1}, (d) 2600–3400 cm^{-1}.

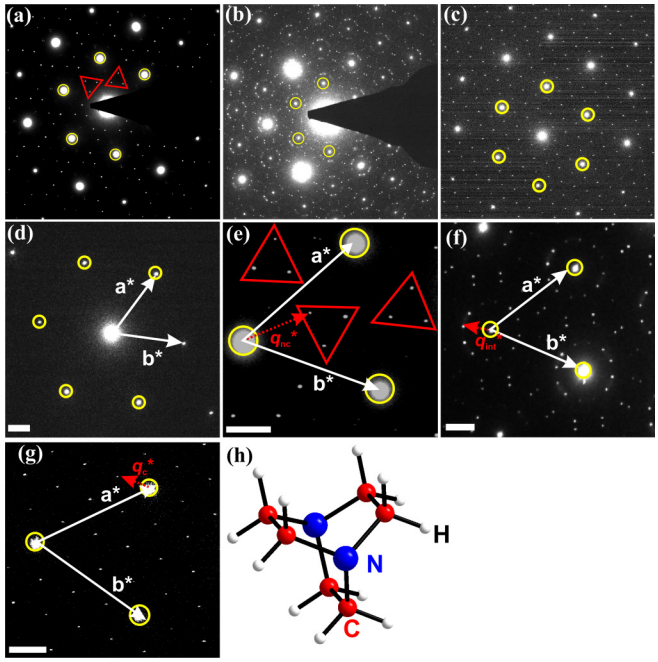

FIG. 3. Electron diffraction pattern from (a) $1T$-TaS_2 at 300 K showing the superlattice spots arising from the nearly commensurate charge density wave (NC-CDW). The circled spots show the spots arising from the main $1T$-TaS_2 structure and the triangles show the superlattice spots (b) TaS_2-TED and (c) $1T$-TaS_2 cooled to ∼90 K and characterized by a commensurate-CDW (C-CDW). Zoomed diffraction pattern showing spots for (d) $2H$-TaS_2 without any superlattice spots (e) $\boldsymbol{q}_{nc}$ in NC-CDW pristine $1T$-TaS_2. (f) $\boldsymbol{q}_{int}$ in intercalated TaS_2-TED. The superlattice spots are enclosed in the circles (g) $\boldsymbol{q}_c$ due to C-CDW pristine $1T$-TaS_2. The superlattice spots are enclosed in the circles .The scale bars in (d)–(g) show a length of $1\,nm^{-1}$. (h) Structure of TED molecule ($C_6H_{12}N_2$).

$1T$-TaS_2 [Fig. 3(a)] is cooled down to 90 K. The structure of the TED molecule ($C_6H_{12}N_2$) is displayed in Fig. 3(h). The electron diffraction pattern from TaS_2-TED [Fig. 3(b)] reveals a complex pattern which differs considerably from the original pattern associated with pristine $1T$-TaS_2 in the NC-CDW phase [Fig. 3(a)]. The modulation wave vector $\boldsymbol{q}_{nc}$ shown in the NC-CDW phase [Fig. 3(d)] is given by $0.245\,\boldsymbol{a}_0^* + 0.068\,\boldsymbol{b}_0^* + \frac{1}{3}\,\boldsymbol{c}_0^*$. On the other hand, in TaS_2-TED the modulation wave vector $\boldsymbol{q}_{int}$ is determined to be $0.2759\boldsymbol{a}_0{}^*$, where $\boldsymbol{a}_0^* = 0.3436\,Å^{-1}$. The value for the modulation wave vector in TaS_2-TED is therefore close to the modulation vector which has been reported in the electron diffraction pattern for mixed polytypes $4Hb$-TaS_2 and $6R$-TaS_2. In particular, we note that the electron diffraction pattern from TaS_2-TED is similar to the diffraction patterns obtained from the mixed polytypes $4Hb$-TaS_2 and $6R$-TaS_2 [1,4,15]. These polytypes are a mixed structure where both $2H$-TaS_2 and $1T$-TaS_2 layers coexist. This is in contrast to $1T$-TaS_2 which is an octahedrally coordinated structure. Furthermore, similar diffraction patterns were reported in $1T$-TaS_2 intercalated with ethylenediamine EDA ($C_2H_8N_2$), hydrazine (N_2H_4) and in $1T$-TaS_2 doped with various metals [1,24,28,32]. In EDA-intercalated TaS_2 the electron diffraction pattern was reported as being first being characterized by a $\sqrt{7}/8\,a_0^* \times \sqrt{7}\,/8\,a_0^*$ superstructure which later transformed into a $\sqrt{13}\,a_0^* \times \sqrt{13}\,a_0^*$ superstructure at room temperature [27,28]. In our case we observe a pattern that matches the $\sqrt{13}\,a_0^* \times \sqrt{13}\,a_0^*$ superstructure. In all these cases, the intercalation process leads to the change in $1T$-TaS_2 stacking to a mixed type of stacking [1]. The agreement of the TaS_2-TED diffraction pattern with those of $4Hb$-TaS_2 and $6R$-TaS_2 polytypes confirms that TaS_2-TED intercalated samples show a structural distortion of some layers with intercalation from octahedral type $1T$ to the trigonal-prismatic coordination ($T \rightarrow H$).

HRTEM investigations of the TaS_2-TED intercalated layers also reveal the structural changes that accompany the intercalation process. Figure 4(a) presents a HRTEM image of TaS_2-TED showing layer structure parallel to the c axis [001]. Atomically resolved two-dimensional (2D) deformation tensor (ε_{ij}) and in-plane rigid-body rotation (ω_{xy}) were then calculated from this HRTEM image. This was done using the established geometrical phase analysis method which can be used to generate atomic-scale strain maps from HRTEM images [45]. The resulting strain maps are displayed in Figs. 4(b)–4(d) showing the in-plane lattice strain ε_{xx}, out of plane strain ε_{yy}, and shear strain ε_{xy}, respectively. Figure 4(e) displays the integrated intensity profiles across the ε_{xx} and ε_{yy} strain maps obtained from the regions marked with dotted rectangles in Figs. 4(b) and 4(c).

These strain profiles show strain values where the positive value is due to tensile strain and negative value due to compressive strain. There are two effects that explain the calculated strain profiles. The first effect is that the intercalation leads to the expansion of the interlayer distance. This leads to the observed strain profiles parallel to the c direction (ε_{yy}) as shown in Figs. 4(c) and 4(e). The second effect is the structural reorganization that follows the intercalation. The electron diffraction and strain analysis presented previously shows that the intercalation process leads from an octahedral to a mixed type or a trigonal-prismatic ($T \rightarrow H$) transformation. In TMDCs, $T \rightarrow H$ interpolytypic transformations occur through a shear transformation process where layers are displaced with respect to each other [15]. In intercalated structure this transformation has been described as glide of the basal plane by $a/\sqrt{3}$ along the $\langle 10\bar{1}0 \rangle$ directions [15,46–48]. This shear transformation process is therefore associated with the formation of planar defects such as stacking faults and associated partial dislocations. These effects result in the shear strain profile ε_{xy} observed in Fig. 4(d). Figure 4(f) presents a HRTEM image of TaS_2-TED showing layer structure parallel to the [100] direction. The respective Fourier transform diffractogram of the HRTEM image is displayed in Fig. 4(g). The diffractogram shows similar CDW modulation as observed in the electron diffraction patterns [see Fig. 3(a)] supporting the conclusion of phase transformation after TED intercalation. However, the information regarding expansion of interlayer distances with intercalation cannot be obtained from Fig. 4(f) as it is obtained perpendicular to layers.

C. Spectral signatures of structural phase transformation due to intercalation

Additionally, the structural effects of the intercalation were also observed in the VEELS spectra. This is presented in

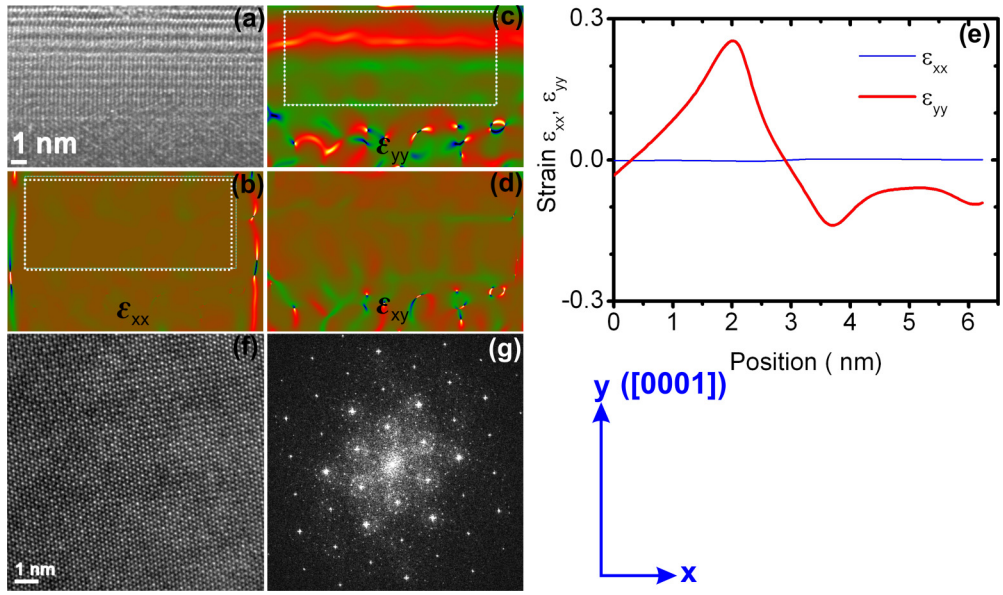

FIG. 4. (a) HRTEM image of TaS_2-TED showing layer structure parallel to the [001] direction. 2D structural deformation maps calculated from the HRTEM image showing (b) in-plane strain ε_{xx}, (c) out of plane strain ε_{yy}, (d) shear strain ε_{xy}. (e) Integrated intensity profiles of ε_{xx} and ε_{yy} strains obtained from the regions marked with dotted rectangles in (b) and (c). (f) HRTEM image of TaS_2-TED showing layer structure parallel to the [100] direction HRTEM. (g) Fourier transform of the HRTEM image in (f) showing the modulation similar to that observed in the electron diffraction patterns.

Fig. 5(a) where we compare experimental VEELS spectra from thin $2H$-TaS_2, $1T$-TaS_2-TED, and $1T$-TaS_2 layers. Various peak features in the spectra have been marked including peak **a*** (0–3 eV), **b***(3–5 eV), **c*** (6–10 eV), **d*** (10–18 eV), and **e***(18–24). The main difference in the VEELS spectra of $1T$-TaS_2 and TaS_2-TED is observed with the increase in the intensity in peak region **b*** (marked with an arrow). In this energy-loss region the VEELS spectrum from TaS_2-TED shows similar peak features to the spectral characteristic of $2H$-TaS_2. In contrast, peak **b*** is missing in the spectra

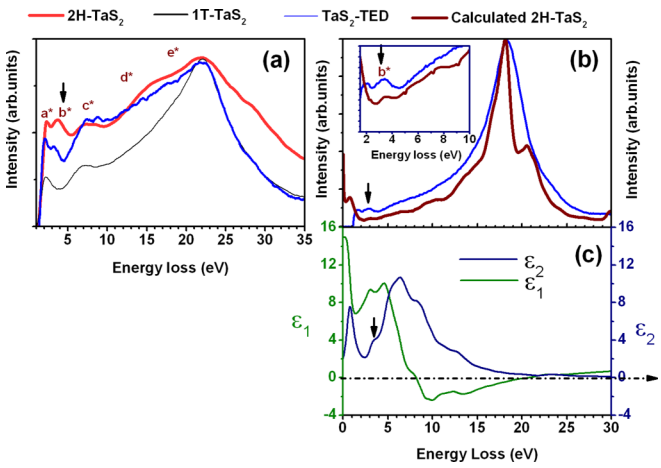

FIG. 5. (a) Comparing the experimental valence electron-energy-loss spectra for $2H$-TaS_2, TaS_2-TED, and $1T$-TaS_2 for very thin layers. (b) Comparing the calculated energy-loss function for $2H$-TaS_2 with that of TaS_2-TED from a thicker layer. The inset shows the energy region encompassing peak **b*** in more details. (c) Imaginary (ε_2) and real part (ε_1) of the dielectric function for $2H$-TaS_2. The peak feature around 3–5 eV is marked with an arrow.

obtained from $1T$-TaS_2. The prominent peaks labeled **c*** and **e*** are observed in all samples. The peaks' features from Ta $O_{2,3}$ edges are also observed in all samples at 40 eV (not shown). Previous studies have shown that peak **e*** corresponds to a plasmon excitation. In this case, the intercalation does not seem to affect the position of the plasmon peak. The extent to which the intercalation process and the associated structural distortions affect features in experimental VEELS spectra was further explored using band-structure calculations and the subsequently calculated EELS spectra. The electron diffraction (Fig. 3) and HRTEM results (Fig. 4) show that intercalation of TED into $1T$-TaS_2 leads to a structural phase transformation. In addition, the experimental VEELS spectra between TaS_2-TED and the trigonal-prismatic $2H$-TaS_2 show similar spectral features. Consequently, we use theoretical calculations based on the trigonal-prismatic phase $2H$-TaS_2 to understand the origin and nature of the spectral features in TaS_2-TED with intercalation. Figure 5(b) compares the calculated spectra for $2H$-TaS_2 with the experimental spectra from intercalated TaS_2-TED obtained from a thicker sample than those displayed in Fig. 5(a). The main motivation to use thicker intercalated layers was to enable a better comparison with calculated spectra. EELS spectra from layered materials can be broadened in very thin samples when compared to a thicker layer. This may lead to some discrepancy in peak intensities when comparing with calculated spectra which are bulklike. However, we note that the peak of interest, peak **b***, is present in all TED intercalated sample regardless of the layer thickness. In addition this peak is absent in pristine, unintercalated $1T$-TaS_2 despite layer thickness. More details regarding the relationship between layer thickness and spectral features are highlighted in the Appendix. While the optical properties of pristine $1T$-TaS_2 and $2H$-TaS_2 have been explored before [49], we go further in our analysis and deter-

mine the nature and origin of the observed spectral features to discuss the changes taking place in intercalated TaS_2-TED. The nature of the observed peaks in the VEELS spectra is best obtained by studying the behavior of the real (ε_1) and imaginary (ε_2) parts of the dielectric function.

Figure 5(c) presents the real (ε_1) and the imaginary parts of the dielectric function (ε_2) for $2H$-TaS_2. These curves are necessary in order to identify the nature of the peaks observed in the experimental VEELS spectra. In the cases where the experimental and calculated spectra match the nature and the character of the peaks observed can then be deduced. The VEELS spectrum is characterized by peaks arising from charge-carrier plasmons, intraband transitions, surface/volume plasmons, and interband transitions. For a metallic system, the intraband and charge-carrier plasmons can be observed at very low energy losses typically <1 eV and therefore do not play a role in our samples. The peaks (**a***, **b***, **c***, **d***, **e***) observed in the experimental VEELS spectra therefore arise from either interband transitions or plasmon excitations. In general, interband transitions lead to peaks being observed in the imaginary part of the dielectric function (ε_2). Plasmon peaks on the other hand correspond to energy positions where the real part of the dielectric function (ε_1) cuts the energy axis with a positive slope with corresponding low value of the ε_2 curve. Based on this analysis peaks **a***, **b***, **c***, and **d*** are interband transitions while peak **e*** is a plasmon peak. In the energy region 3–5 eV the ε_2 curve from the $2H$-TaS_2 phase is characterized by a peak feature marked with an arrow. We note that this is the same energy region that corresponds to peak **b*** observed in the TaS_2-TED VEELS spectra. According to the literature [38–40], the features in this energy range can be ascribed to interband transitions, which are more intense in the trigonal-prismatic phase $2H$-TaS_2, and TaS_2-TED and are less intense in the octahedral $1T$-TaS_2 phase. In the following discussion we use the calculated full and partial ε_2 spectra and the band structure to determine the origin of and nature of these interband transitions. Figures 6(a)–6(d) present the band-structure plots of $2H$-TaS_2 showing the $S-p$, $Ta 5dx^2-y^2+5dxy$, $5dxz+5dyz$, and $Ta-5dz^2$ character of the bands, respectively.

The character of the respective bands is represented by a sphere, where the radius of the sphere is related to the d or p character in a respective band. In the band-structure plot [Fig. 6(a)], a set of bands numbered 27, 31, 34, 38, 39 and 41, 45, 50, 55, 60 have been labeled. Bands numbered 27, 31, 35, and 38 have a significant S-3 p character. On the other hand, bands 39 and 41 show mainly Ta-5 d character. This is also the case with other bands at the bottom of the valence band. The band structure and associated theoretical EELS spectra calculations allow for the determination of the origin and the nature of interband transitions, which are observed in the valence energy-loss spectra. This is possible because the ELF which is equivalent to the single scattered VEELS spectra can be expressed as $\mathrm{ELF} = \mathrm{Im}(-\varepsilon^{-1}) = \varepsilon_2/({\varepsilon_1}^2+{\varepsilon_2}^2)$ where ε, ε_1, and ε_2 are the dielectric function, real and imaginary parts of the dielectric function, respectively [38,39]. The advantage of this theoretical approach is that it enables partial ε_2 functions to be calculated. These partial ε_2 curves are calculated by decomposing the calculated ε_2 function into a pair or a group

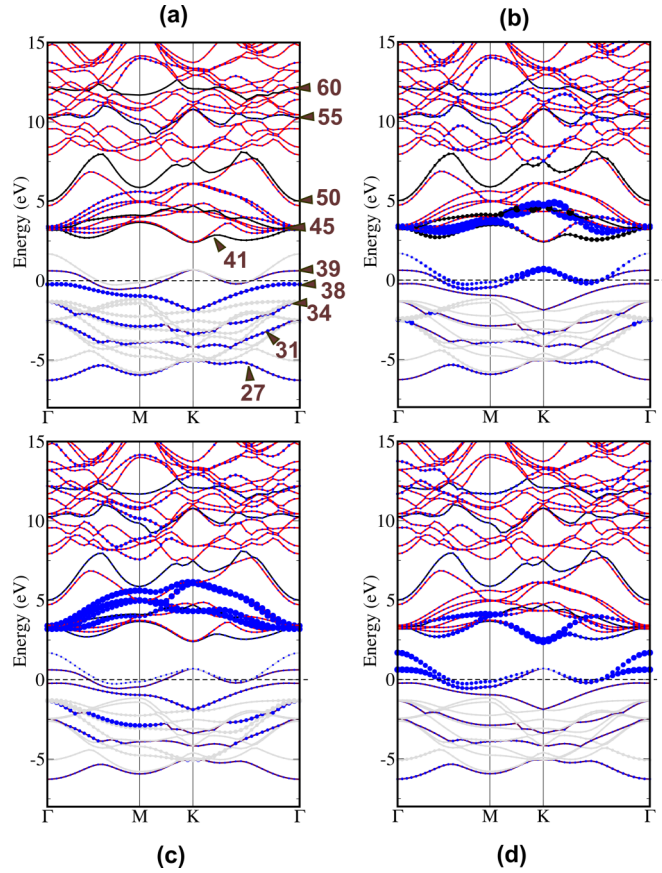

FIG. 6. Calculated band structure of $2H$-TaS_2 showing the character of the bands for (a) S-3p with select maroon colored bands 27, 31, 34, 38, 39 and black colored bands 41, 45,50,55, 60 labeled. (b) $Ta-5dx^2-y^2+5dxy$. (c) $Ta-5dxz+5dyz$. (d) $Ta-5dz^2$. The character of the bands is represented by a sphere where the radius of the sphere is related to the d or p character in a respective band.

of valence and conduction bands contributing to peaks in the ε_2 curve. This allows for the assignment of the peak features in the VEELS spectra to specific interband transitions as well as their S-3 p or Ta-5 d character. Figures 7(a)–7(f) show the calculated partial ε_2 curves involving the interband transitions arising from the marked bands 27, 31, 34, 38, 39, respectively, to the unoccupied bands 41, 45, 50, 55, 60. The lowest interband transitions consist of transitions from band 38 to bands with mainly Ta-5 d character and which are located at/near the Fermi level. These transitions make contributions to peaks found at energies up to 2 eV. Transitions involving band 38 to band 41 make the most contribution to the peaks between 2 and 5 eV. From the band-structure plot [Fig. 6(a)] we also observe that band 38 has an S-3 p character. Band 41 on the other hand has mainly metallic Ta-5 d character. Interband transitions from band 38, which also contribute to peaks observed between 2–5 eV, are mainly of ligand-metal charge-transfer transitions, since they originate from states with mainly ligand (S-3 p) character to states with mainly metallic character (Ta-5 d) at the bottom of the conduction band.

In the following, we briefly discuss these theoretical results in the context of the structural transformation accompanying

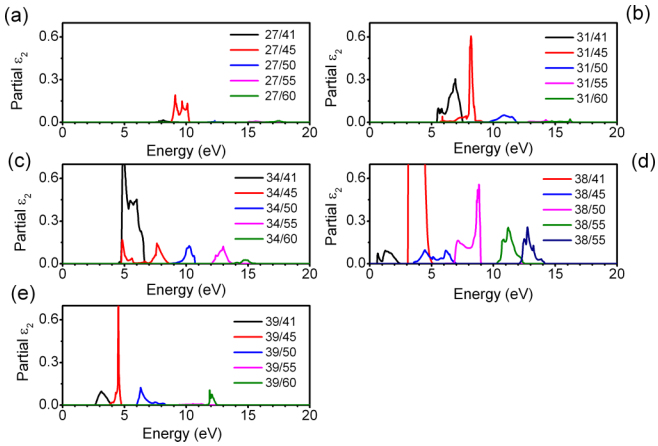

FIG. 7. Partial ε_2 function calculated for interband transitions from occupied bands (a) 27, (b) 31, (c) 34, (d) 38 (e) 39 to the unoccupied bands 41, 45, 50, 55, 60.

the intercalation, as observed in the experiment. It is well known that the electronic structure of the TMDC is strongly affected by the changes in the coordination of the transition metal ion. In general, the octahedral (1*T*) symmetry is characterized by degenerate orbitals of the symmetry $e_g(d_{z^2}, d_{x^2-y^2})$ and $t_{2g}(d_{xy}, d_{yz}, d_{xz})$ [1,50,51]. On the other hand, the trigonal-prismatic phase is characterized by three groups of orbitals, $a_1({}_zd_2)$, $e'(d_{x^2-y^2} + d_{xy})$, and $e''(d_{yz} + d_{xz})$. In the trigonal-prismatic structure the dz [2] band is shifted to lower energies with respect to the $d_{x^2-y^2}$, d_{xy}, d_{yz}, and d_{xz} bands. Additionally, the d bands (d manifold) in the trigonal-prismatic coordination are shifted to lower energies in comparison to the d bands in the octahedral coordination case. This is schematically shown in Fig 8.

Here, the bands a_{1g}, t_{1u}, and a_2'' with mainly S-3 p character are also indicated. The arrows show the possible charge-transfer (p-d) interband transitions. Accordingly, the charge-transfer interband transitions will be shifted to lower energies in the trigonal-prismatic coordination compared to those in the octahedral coordination. This leads to a higher

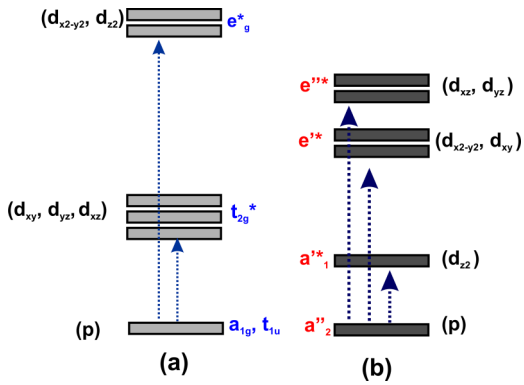

FIG. 8. Schematic showing the general trend in the band structure between (a) octahedral and (b) trigonal-prismatic structures [1,56]. The dotted arrows represent possible charge-transfer interband transitions

intensity in the lower energy-loss region of the trigonal-prismatic phase. The equivalent transitions in the octahedral phase would appear at a higher energy loss. In addition, the overlap between metal and chalcogen orbitals is optimized in the trigonal-prismatic structure resulting in a higher degree of covalency [1]. The observation of higher peak intensities in the VEELS spectra of intercalated TaS_2 is therefore a reflection of the electronic band-structure changes accompanying the $T \rightarrow H$ phase transformation. These include variations in transition probability, covalency, and shifts in peak positions [52–55]. The probability of a transition is proportional to the density of the unoccupied final states and the matrix element representing the degree of overlap between the initial and the final state [40]. Within the dipole approximation, the probability of a transition is therefore higher if the density of unoccupied final states being probed by the transition is large. This is then reflected in a higher intensity of the allowed transition. Variation in the degree of covalency can also affect the intensity of peaks arising from interband transition in VEELS. The intensity associated with charge-transfer interband transitions from filled ligand orbitals to partially occupied metallic orbitals also reflects the character of the metal-ligand bonding. The intensity of these charge-transfer transitions is proportional to $(RS_{\text{overlap}})^2$, where S_{overlap} is the overlap of the donor and acceptor orbitals and the R is the metal-ligand bond length [51,52]. The intensity of a charge-transfer transition is therefore higher with increasing overlap between the metal and the ligands. The octahedral to trigonal-prismatic phase transition with intercalation is therefore associated with a shift in the energy of the d manifold to lower energies [1,50,55]. In addition, the trigonal-prismatic phase is more covalent than the octahedral phase [1]. These two effects become significant in the intercalated sample due to the associated structural transformation. This leads to the observed increase in peak intensity of the VEELS spectra with intercalation.

IV. CONCLUSIONS

In conclusion, we have investigated the changes in the atomic and electronic structure of 1*T*-TaS_2 due to intercalation with triethylenediamine ($C_6H_{12}N_2$). We show that the intercalation process leads to strong modifications in the atomic, electronic, and the CDW/PLD structure in intercalated TaS_2 at room temperature. This is characterized by a structural transformation of some layers from the octahedral to a trigonal-prismatic coordination. This structural phase transformation with the intercalation is also reflected in the valence electron-energy-loss spectra. Increased peak intensity is observed in the energy-loss region between 3–5 eV on the VEELS spectra of the intercalated sample due to this structural transformation. Using band-structure calculations we determine the nature of this peak to be an interband transition from mainly ligandlike states (S-3 p) in the conduction band to mainly metallic states (Ta-5 d) in the valence band. The increase in the intensity of this peak with intercalation is interpreted to arise from higher transition probability due to an increase in covalency as well a shift in the energy of the d manifold to lower energies as a result of structural changes accompanying the intercalation.

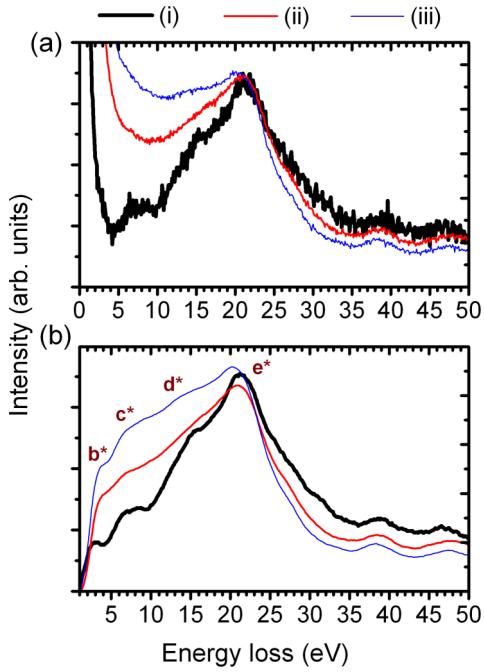

FIG. 9. (a) Experimental EELS from $2H$-TaS_2 for increasing sample thickness (i)<(ii)<(iii). (b) EELS spectra after elastic peak subtraction showing the positions of various peaks.

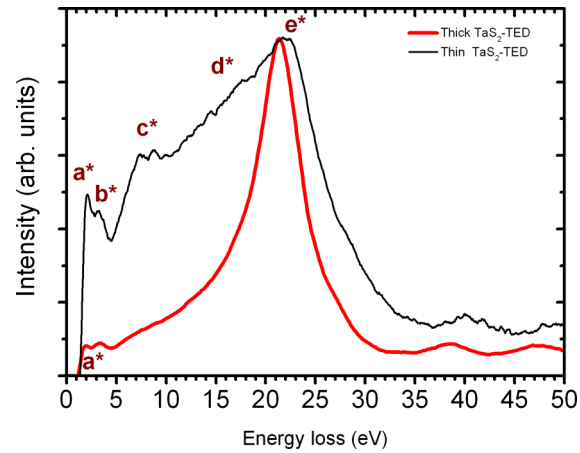

FIG. 10. Comparison of measured EELS spectra obtained from a thick TaS_2-TED sample (thick red curve) to that of a very thin sample (thin black curve).

ACKNOWLEDGMENTS

The authors acknowledge funding from the Deutsche Forschungsgemeinschaft (DFG) and the Ministry of Science, Research and the Arts (MWK) of the federal state Baden-Württemberg, Germany in the frame of the SALVE (Sub-Angstroem Low-Voltage) project.

APPENDIX: EFFECTS OF SURFACE EXCITATIONS

In our paper we used the calculated spectra for $2H$-TaS_2, in order to understand the origin and nature of the peaks observed in the experimental EELS spectra for $2H$-TaS_2 and TaS_2-TED. A comparison of both sets of spectra [Figs. 5(a) and 5(b)] show that the experimental spectra [Fig. 5(a)] from very thin layers are broadened in comparison to the calculated spectra as well as from thicker layers [Fig. 5(b)]. This is because experimental EELS spectra were obtained from very thin flakes and the effects of the surface increase in such spectra. The calculated spectra on the other hand are obtained from bulk structures and hence the spectra are not broadened. In Fig. 9(a) we present experimental spectra obtained $2H$-TaS_2 for increasing sample thickness (iii)>(ii)>(i). The broadening of the spectra with decreasing sample thickness can be clearly observed. According to Fig. 9(b), all features are present in the spectra regardless of the sample thickness. Therefore, the peaks found in our spectra are not due to surface effects but are characteristic for the samples being investigated. These peaks are therefore interband transitions and volume plasmons. Similarly, in Fig. 10 we also show experimental spectra obtained for a thick (thick red curve) and very thin (thin black curve) TaS_2-TED sample. The broadening of the spectra with decreasing sample thickness can be clearly observed. However, all peak features are reproduced in both thick and thin samples including peak **b***, which we interpret as a signature for the structural phase transformation.

[1] J. A. Wilson, F. J. Di Salvo, and S. Mahajan, Adv. Phys. **24**, 117 (1975); J. A. Wilson and A. D. Yoffe, *ibid.* **18**, 193 (1969).
[2] R. H. Friend and D. Jerome, J. Phys. C **12**, 1441 (1979).
[3] R. L. Withers and J. A. Wilson, J. Phys. C **19**, 4809 (1986).
[4] P. M. Williams, C. B. Scruby, W. B. Clark, and G. S. Parry, J. Phys. Colloq. **37**, C4-139 (1976).
[5] C. B. Scruby, P. M. Williams, and G. S. Parry, Philos. Mag. **31**, 255 (1975).
[6] G. Grüner, Rev. Mod. Phys. **60**, 1129 (1988).
[7] H. Dai and C. Lieber, Annu. Rev. Phys. Chem. **44**, 237 (1993).
[8] T. Ishiguro and H. Sato, Phys. Rev. B **52**, 759 (1995).
[9] A. W. Tsen, R. Hovden, D. Wang, Y. D. Kim, J. Okamoto, K. A. Spoth, Y. Liu, W. Lu, Y. Sun, J. C. Hone, L. F. Kourkoutis, P. Kim, and A. N. Pasupathy, Proc. Natl. Acad. Sci. USA **112**, 15054 (2015).
[10] D. Sakabe, Z. Liu, K. Suenaga, K. Nakatasugawa, and S. Tanda, NPJ Quantum Mater. **2**, 22 (2017).
[11] R. Brouwer and F. Jellinek, Physica (Amsterdam) B+C **99**, 51 (1980).
[12] A. Spijkerman, J. L. de Boer, A. Meetsma, G. A. Wiegers, and S. van Smaalen, Phys. Rev. B **56**, 13757 (1997).
[13] D. E. Moncton, J. D. Axe, and F. J. DiSalvo, Phys. Rev. Lett. **34**, 734 (1975).
[14] P. Monceau, Adv. Phys. **61**, 325 (2012).
[15] J. van Landuyt, G. van Tendeloo, and S. Amelinckx, Phys. Status Solidi A **26**, 359 (1974); **26**, 585 (1974); **36**, 757 (1976).
[16] H. Katzke, P. Toledano, and W. Depmeier, Phys. Rev. B **69**, 134111 (2004).
[17] E. Fradkin, S. A. Kivelson, and J. M. Tranquada, Rev. Mod. Phys. **87**, 457 (2015).

[18] B. Keimer, S. A. Kivelson, M. R. Norman, S. Uchida, and J. Zaanen, Nature (London) **518**, 179 (2015).

[19] J. Chang, E. Blackburn, A. T. Holmes, N. B. Christensen, J. Larsen, J. Mesot, R. Liang, D. A. Bonn, W. N. Hardy, A. Watenphul, M. v. Zimmermann, E. M. Forgan, and S. M. Hayden, Nat. Phys. **8**, 871 (2012).

[20] G. Ghiringhelli, M. Le Tacon, M. Minola, S. Blanco-Canosa, C. Mazzoli, N. B. Brookes, G. M. De Luca, A. Frano, D. G. Hawthorn, F. He, T. Loew, M. M. Sala, D. C. Peets, M. Salluzzo, E. Schierle, R. Sutarto, G. A. Sawatzky, E. Weschke, B. Keener, and L. Braicovich, Science **337**, 821 (2012).

[21] E. Morosan, H. W. Zandbergen, B. S. Dennis, J. W. G. Bos, Y. Onose, T. Klimczuk, A. P. Ramirez, N. P. Ong, and R. J. Cava, Nat. Phys. **2**, 544 (2006).

[22] H.-H. Kim, S. M. Souliou, M. E. Barber, E. Lefrancois, M. Minola, M. Tortora, R. Heid, N. Nandi, R. A. Borzi, G. Garbarino *et al.*, Science **362**, 1040 (2018).

[23] K. Cho, M. Konczykowski, S. Teknowijoyo, M. A. Tanatar, J. Guss, P. B. Gartin, J. M. Wilde, A. Kreyssig, R. J. McQueeney, A. I. Goldman, V. Mishra, P. J. Hirschfeld, and R. Prozorov, Nat. Commun. **9**, 2796 (2018).

[24] S. F. Meyer, B. E. Howard, G. R. Stewart, J. V. Acrivos, and T. H. Geballe, J. Chem. Phys. **62**, 4411 (1975).

[25] R. H. Friend and A. D. Yoffe, Adv. Phys. **36**, 1 (1987).

[26] F. R. Gamble, J. H. Osiecki, M. Cais, R. Pishahordy, F. J. DiSalvo, and T. H. Geballe, Science **174**, 493 (1971); F. R. Gamble, F. J. DisSalvo, R. A. Klemm, and T. H. Geballe, *ibid.* **168**, 568 (1970).

[27] A. M. Ghorayeb, W. Y. Liang, and A. D. Yoffe, J. Phys. C: Solid State Phys. **19**, 7323 (1986); A. M. Ghorayeb, and R. H. Freund, J. Phys.: Condens. Matter. **6**, 3533 (1994).

[28] G. J. Tatlock and J. V. Acrivos, Philos. Mag. B **38**, 81 (1978).

[29] A. R. Beal and W. Y. Liang, J. Phys. C: Solid State Phys. **6**, L482 (1973); A. R. Beal, *ibid.* **11**, 4583 (1978); A. R. Beal, H. P. Hughes, and W. Y. Liang, *ibid.* **8**, 4236 (1975); A. R. Beal, and W. Y. Liang, Philos. Mag. **27**, 1397 (1973).

[30] P. Ganal, W. Olberding, T. Butz, and G. Ouvrard, Solid State Ionics **59**, 313 (1993); P. Ganal, T. Butz, W. Karle, K.-H. Spiedel, and A. Lerf, Hyperfine Interact. **60**, 903 (1990); P. Ganal, M. Evain, R. Brec, and T. Butz, Mater. Sci. Forum **91-93**, 225 (1992).

[31] E. A. Marseglia, Int. Rev. Phys. Chem. **3**, 177 (1983).

[32] W. B. Clark and P.M Williams, Philos. Mag. **35**. 883 (1977).

[33] G. S. Parry, C. B. Scruby, and P. M. Williams, Philos. Mag. **29**, 601 (1974).

[34] C. Pettenkofer and W. Jaegermann, Phys. Rev. B **50**, 8816 (1994).

[35] A. V. Powell, Annu. Rep. Prog. Chem. C **90**. 177 (1993).

[36] R. Manzke, G. Crecelius, J. Fink, and R. Schöllhorn, Solid State Commun. **40**, 103 (1981).

[37] M. Sarma, A. R. Beal, S. Nulsen, and R. Friend, J. Phys. C **15**, 477 (1982).

[38] J. Fink, Adv. Electron. Electron Phys. **75**, 121 (1989).

[39] R. F. Egerton, Rep. Prog. Phys. **72**, 016502 (2009).

[40] R. Bringans, W. Y. Liang, and R. D. Bringans, J. Phys. C: Solid State Phys. **14**, 1053 (1981).

[41] C. Ambrosch-Draxl and J. O. Sofo, Comput. Phys. Commun. **175**, 1 (2006).

[42] G. S. Weiss, A. S. Parkes, E. R. Nixon, and R. E. Hughes, J. Chem. Phys. **41**, 3759 (1964).

[43] M. P. Marzocchi, G. Sbrana, and G. Zerbi, J. Am. Chem. Soc. **87**, 1429 (1965).

[44] P. Brüesch and Hs. H. Günthard, Spectrochim. Acta **22**, 877 (1966).

[45] M. Hytch, E. Snoeck, and R. Kilaas, Ultramicroscopy **74**, 131 (1998).

[46] G. C. Trigunayat, Solid State Ionics **48**, 3 (1991).

[47] M. Remskar, A. Popovic, and H. I. Starnberg, Surf. Sci. **430**, 199 (1999).

[48] M. Sidorov, M. McKelvy, R. Sharma, W. Glausinger, P. Ganal, P. Moreau, and G. Ouvrard, Chem. Mater. **7**, 1140 (1995).

[49] M. G. Bell and W. Y. Liang, Adv. Phys. **25**, 53 (1976).

[50] L. F. Matheiss, Phys. Rev. B, **8**, 3719 (1973).

[51] R. Huisman, R. De Jonge, C. Haas, and F. Jellinek, J. Solid State Chem. **3**, 56 (1971).

[52] T. Glaser, B. Hedman, K. O. Hodgson, and E. I. Solomon, Acc. Chem. Res. **33**, 859 (2000).

[53] E. I. Solomon, D. W. Randall, and T. Glaser, Coord. Chem. Rev. **200–202**, 595 (2000).

[54] A. van der Avoird and P. Ros, Theor. Chim. Acta (Berlin) **4**, 13 (1966).

[55] P. Moreau, V. Mauchamp, F. Pailloux, and F. Boucher, Appl. Phys. Lett. **94**, 123111 (2009).

[56] D. Pasquier and O. V. Yazyev, 2D Materials **6**, 025015 (2019).